

# Low-dimensional metal-organic magnets as a route towards the $S = 2$ Haldane phase

Jem Pitcairn,<sup>†</sup> Andrea Iliceto,<sup>‡</sup> Laura Cañadillas-Delgado,<sup>¶</sup> Oscar Fabelo,<sup>¶</sup> Cheng Liu,<sup>§</sup> Christian Balz,<sup>||</sup> Andreas Weilhard,<sup>†</sup> Stephen P. Argent,<sup>†</sup> Andrew J. Morris,<sup>‡</sup> and Matthew J. Cliffe<sup>\*,†</sup>

<sup>†</sup>*School of Chemistry, University of Nottingham, University Park, Nottingham, NG7 2RD, United Kingdom*

<sup>‡</sup>*School of Metallurgy and Materials, University of Birmingham, Edms Rd, Edgbaston, Birmingham B15 2TT, United Kingdom*

<sup>¶</sup>*Institut Laue-Langevin, 71 avenue des Martyrs - CS 20156, 38042 Grenoble, France*

<sup>§</sup>*Cavendish Laboratory, Department of Physics, University of Cambridge, JJ Thomson Avenue, Cambridge CB3 0HE, United Kingdom*

<sup>||</sup>*ISIS Neutron and Muon Source, STFC Rutherford Appleton Laboratory, Harwell Oxford, Didcot OX11 0QX, United Kingdom*

E-mail: matthew.cliffe@nottingham.ac.uk

## Abstract

Metal-organic magnets (MOMs), modular magnetic materials where metal atoms are connected by organic linkers, are promising candidates for next-generation quantum technologies. MOMs readily form low-dimensional structures, and so are ideal systems to realise physical examples of key quantum models, including the Haldane phase, where a topological excitation gap occurs in integer-spin antiferromagnetic (AFM) chains.

Thus far the Haldane phase has only been identified for  $S = 1$ , with  $S \geq 2$  still unrealised because the larger spin imposes more stringent requirements on the magnetic interactions. Here, we report the structure and magnetic properties of  $\text{CrCl}_2(\text{pym})$  (pym=pyrimidine), a new quasi-1D  $S = 2$  AFM MOM. We show, using X-ray and neutron diffraction, bulk property measurements, density-functional theory calculations and inelastic neutron spectroscopy (INS) that  $\text{CrCl}_2(\text{pym})$  consists of AFM  $\text{CrCl}_2$  spin chains ( $J_1 = -1.13(4)$  meV) which are weakly ferromagnetically coupled through bridging pym ( $J_2 = 0.10(2)$  meV), with easy-axis anisotropy ( $D = -0.15(3)$  meV). We find that although small compared to  $J_1$ , these additional interactions are sufficient to prevent observation of the Haldane phase in this material. Nevertheless, the proximity to the Haldane phase together with the modularity of MOMs suggests that layered Cr(II) MOMs are a promising family to search for the elusive  $S = 2$  Haldane phase.

# Introduction

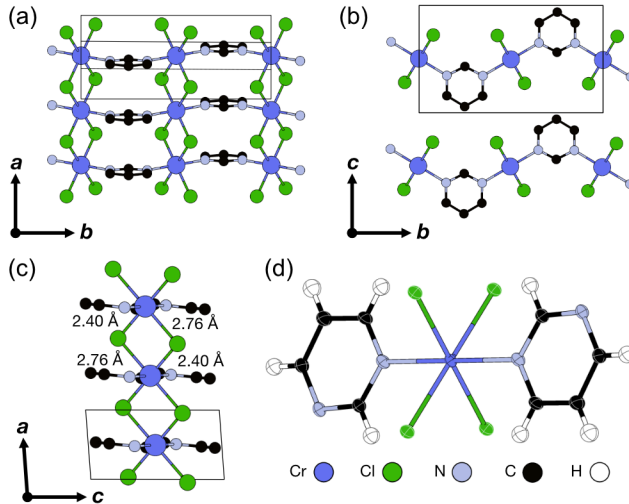


Figure 1: Crystal structure of  $\text{CrCl}_2(\text{pym})$  viewed along the (a)  $c$ , (b)  $a$  and (c)  $b$  axes. Cr-Cl bond lengths are labelled and H atoms are omitted for clarity. (d) ORTEP diagram showing the coordination environment.

Metal-organic magnets (MOM) are assembled from metal nodes bridged by organic molecular linkers into extended networks.<sup>1</sup> This gives them a number of advantages over conven-

tional inorganic magnets: there is a much wider diversity of organic than atomic ligands;<sup>2</sup> the modularity of their construction allows for tuning of interactions while retaining the topology<sup>3</sup> and their longer lengths facilitate magnetic low-dimensionality,<sup>4,5</sup> and thus enhanced quantum fluctuations.<sup>6</sup> Perhaps most excitingly, it has recently been demonstrated that redox-active radical ligands can introduce into MOFs both high electronic conductivity ( $0.45 \text{ Scm}^{-1}$ )<sup>7</sup> and strong magnetic interactions,<sup>8,9</sup> despite the long-distances between metal centres. This suggests that MOMs could form the basis for practical new quantum technology.<sup>10–14</sup>

MOM spin chains are now well established as host materials for distinctively quantum behaviour, from spin fractionalisation in  $\text{Cu}(\text{C}_6\text{H}_5\text{COO})_2 \cdot 3\text{H}_2\text{O}$ <sup>15</sup> to the quantum sine-Gordon physics of  $\text{Cu}(\text{pym})(\text{NO}_3)(\text{H}_2\text{O})_2$ <sup>16</sup> and  $[\text{Cu}(\text{pym})(\text{H}_2\text{O})_4]\text{SiF}_6 \cdot \text{H}_2\text{O}$ .<sup>17</sup> One of the most striking quantum discoveries in MOMs was the measurement of the topological Haldane gap in the antiferromagnetic  $S = 1$  spin chain MOM  $\text{Ni}(\text{C}_2\text{H}_8\text{N}_2) \cdot 2\text{NO}_2(\text{ClO}_4)$ <sup>18–20</sup> and subsequent efforts have uncovered a number of other high-quality model systems.<sup>21–24</sup> The Haldane phase is yet to be experimentally realised for spins  $S > 1$ .

The difficulty of reaching the Haldane phase for  $S \geq 2$  is largely because the size of the Haldane gap relative to the intrachain exchange,  $\Delta/J_1$ , decreases significantly from  $\Delta/J_1 = 0.41$  for  $S = 1$  to  $\Delta/J_1 = 0.087$  for  $S = 2$ , making the gap both more sensitive to the presence of single-ion anisotropy and non-Heisenberg exchange interactions, and harder to detect when present.<sup>25</sup> These challenges have meant that although AFM  $S = 2$  spin chains which could be candidates to host the Haldane phase have been identified, the  $S = 2$  gap has not yet been observed.<sup>26–30</sup> The combination of modularity and low-dimensionality of MOMs means they are an ideal platform to search for the  $S = 2$  Haldane phases. However, the most synthetically accessible  $S = 2$  transition metal ion is  $\text{Fe}^{2+}$ , which typically possesses large single ion anisotropy due to its partially quenched  $^5T_{2g}$  ground state, and other  $S = 2$  ions,  $\text{Mn}^{3+}$  and  $\text{Cr}^{2+}$ , are usually sensitive to reduction or oxidation in ambient conditions. As a result, the chemistry of MOMs which could host  $S = 2$  Haldane phases is comparatively

underexplored, and their quantum states thus unrealised.

Here we report  $\text{CrCl}_2(\text{pym})$ , a new 2D layered magnetic coordination polymer consisting of  $\text{CrCl}_2$  chains bridged by pym ligands with a structure analogous to that of the other transition metal monopyrimidine chlorides ( $\text{MCl}_2(\text{pym})$ ,  $\text{M} = \text{Mn, Fe, Co, Ni, Cu}$ ),<sup>31</sup> the Mn, Co and Cu analogues of which are reported to possess antiferromagnetic coupling without order down to 1.8 K.<sup>32</sup> We first describe its synthesis and structural characterisation using X-ray diffraction, where the presence of a pronounced Jahn-Teller (JT) distortion confirms the presence of  $\text{Cr}^{2+}$ . We then go on to show using comprehensive magnetic characterisation, including bulk magnetisation, heat capacity measurements, powder neutron diffraction (PND) and powder inelastic neutron scattering (INS) measurements of fully protonated samples, that  $\text{CrCl}_2(\text{pym})$  orders into a Néel ground state at  $T_N = 20.0(3)$  K, with AFM ordering along the  $\text{CrCl}_2$  chain, FM coupling of the chains through pym and interlayer FM correlations. Through detailed analysis of the neutron scattering data, in combination with density-functional theory (DFT) calculations, we quantitatively determine the size of the key magnetic interactions, which suggest that  $\text{CrCl}_2(\text{pym})$  is a well separated  $S = 2$  AFM with near isotropic single ion properties. We therefore suggest that through careful ligand choice this family of MOMs offers a potential route to realise the Haldane phase for  $S = 2$ .

## Results

### Synthesis and structure

We synthesised  $\text{CrCl}_2(\text{pym})$  by reacting  $\text{CrCl}_2$  with pyrimidine. We found that the monopyrimidine  $\text{CrCl}_2(\text{pym})$  forms in a wide variety of solvents and stoichiometries, and even *via* neat combination and with excess ligand, although bispyrimidine analogues are known for other transition metals.<sup>33–35</sup> Single crystals suitable for X-ray diffraction measurements were grown through vapour diffusion. We solved the structure from single-crystal X-ray diffraction (SCXRD) data and found that  $\text{CrCl}_2(\text{pym})$  crystallises in the monoclinic space group

$P2_1/m$  with two formula units in the unit cell (Tab. S1). The  $\text{Cr}^{2+}$  are coordinated by four  $\text{Cl}^-$  ligands and two N atoms from the pyrimidine ligands, which forms a distorted  $\text{CrCl}_4\text{N}_2$  octahedron (Fig. 1c & d). The chromium octahedra edge-share through the  $\text{Cl}^-$  ligands along the crystallographic  $a$  direction, and these chains are connected by pyrimidine ligands along the crystallographic  $b$  direction with an alternating orientation to form corrugated layers (Fig. 1a). These layers stack in the crystallographic  $c$  direction through van der Waals interactions (Fig. 1b). The  $\text{Cr}^{2+}$  ion has a large JT distortion, with a long  $\text{Cr}-\text{Cl}$  bond length of  $d_{\text{Cr}-\text{Cl}} = 2.761(5) \text{ \AA}$ , comparable to the complex  $\text{Cr}^{2+}\text{Cl}_2(\text{pyridine})_4$   $d_{\text{Cr}-\text{Cl}} = 2.803(1) \text{ \AA}$ ,<sup>36</sup> confirming the  $\text{Cr}^{2+}$  oxidation state. Powder X-ray diffraction performed after exposure to air for one month show the lattice distortion resulting from this JT distortion is retained, demonstrating that the bulk of the sample maintains the  $\text{Cr}^{2+}$  oxidation state after exposure to air (Fig. S4).

## Magnetic susceptibility

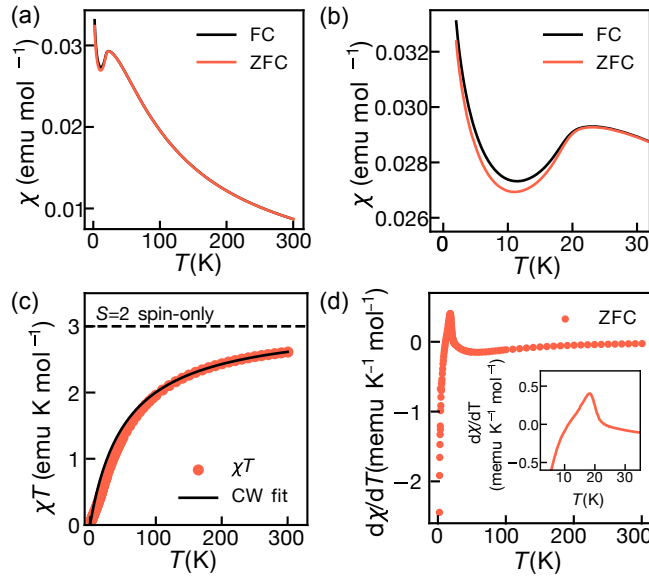


Figure 2: Magnetic susceptibility,  $\chi$ , measurements of  $\text{CrCl}_2(\text{pym})$ . (a)  $\chi(T)$  measured in zero-field cooled (ZFC) and field cooled (FC) conditions from 2–300 K. (b)  $\chi(T)$  data highlighted for 2–30 K. (c)  $\chi T(T)$  in ZFC and FC conditions 2–300 K, with Curie-Weiss fit carried out over  $300 > T > 150$  K. Dashed line shows the  $S = 2$  spin-only limit. (d) ZFC  $\frac{d\chi}{dT}(T)$  over 2–300 K. Inset: ZFC  $\frac{d\chi}{dT}(T)$  over 2–35 K.

As we expected  $\text{CrCl}_2(\text{pym})$  to be an  $S = 2$  2D magnet, we measured its temperature dependent magnetic susceptibility,  $\chi(T)$ . The sample was measured under field cooled (FC) and zero-field cooled (ZFC) conditions in a 0.01 T *dc* field from 2 K to 300 K. These data show a broad peak at 20-25 K characteristic of short-range ordering and low-dimensional magnetism (Fig. 2a). The  $\frac{d\chi}{dT}(T)$  data show a discontinuity at 20 K, indicating a phase transition from a disordered magnetic state to a long-range ordered AFM state (Fig. 2d). Fitting  $\chi^{-1}(T)$  data to the Curie-Weiss law gave a Curie constant,  $C = 3.08(1)$  emu K mol $^{-1}$ , in good agreement with the presence of high-spin  $\text{Cr}^{2+}$  ( $C = 3$  emu K mol $^{-1}$ ) (Fig. 2c & d). The Curie-Weiss temperature is significant and negative,  $\theta = -54.1(5)$  K, indicating net antiferromagnetic interactions (Fig. 2d), and isothermal magnetisation measurements carried out at 2 K show that saturation is not reached at fields of 5 T (Fig. S7). While  $M(H)$  is linear in  $\mu_0 H > 1$  T, there is a small sigmoid feature at  $\mu_0 H < 1$  T consistent with minor paramagnetic impurities.

The rise in  $\chi(T)$  below  $T = 10$  K indicates the presence of small quantities of paramagnetic spins, which we determined to be 1.1(1) spin % from fitting of the Curie-like tail (Fig. S13).<sup>37</sup> This Curie-like tail may be caused free-spins at chain-ends or  $\text{Cr}^{3+}$  formed due to surface oxidation (Fig. 2b). Indeed, measurement of the magnetic susceptibility of  $\text{CrCl}_2(\text{pym})$  after air exposure showed a large increase in the paramagnetic contribution, 15.0(2) spin % (Fig. S6), and X-ray photoelectron spectroscopy (XPS) of this air-exposed sample primarily detected oxidised Cr (Fig. S8), with  $\text{Cr}^{3+}$ ,  $\text{Cr}^{6+}$  and metallic Cr present, as well as O 1s peaks consistent with the formation of  $\text{Cr}(\text{OH})_3$ .<sup>38</sup>

## Heat capacity

The molar heat capacity,  $C_p(T)$ , of  $\text{CrCl}_2(\text{pym})$  was measured from 2–60 K. We found a peak in  $C_p(T)$  occurred at 20.0(3) K (Fig. 3a), consistent with the magnetic phase transition observed in the magnetic susceptibility data (Fig. 2a). We obtained an estimate of the entropy of magnetic ordering by integrating  $C_p/T(T)$  after subtraction of a linear background

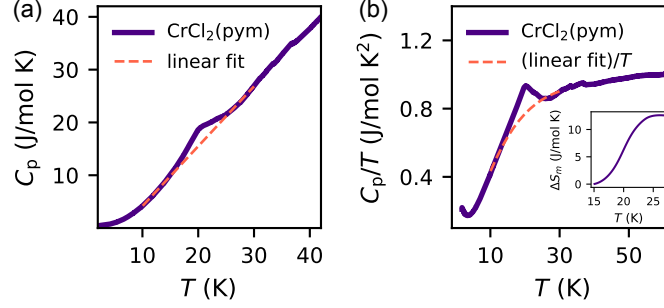


Figure 3: (a) Heat capacity as a function of temperature,  $C_p(T)$ , with the non-magnetic background approximated by a linear fit over the region 10 to 30 K (dashed). (b)  $C_p/T(T)$ , with non-magnetic background (dashed). Inset: entropy near  $T_N$ .

(10 – 15 K and 27 – 30 K)(Fig. 3b), to account for phononic contributions. We found that the measured value of magnetic entropy ( $S_{\text{exp.}} = 12.7(4) \text{ Jmol}^{-1}\text{K}^{-1}$ ) is slightly reduced from the expected value ( $S_{\text{calc.}} = 13.4 \text{ Jmol}^{-1}\text{K}^{-1}$ ). The small features present in the data between 30–40 K are due to instrumental error.

## Neutron Diffraction

Our bulk measurements thus strongly suggested the presence of long-range magnetic order. To determine the nature of this magnetic ground state we carried out PND using instrument D1B at the ILL on a 5 g non-deuterated sample of  $\text{CrCl}_2(\text{pym})$ . We measured the neutron diffraction pattern at two temperatures:  $T = 1.5 \text{ K}$  below  $T_N$ , and  $T = 30 \text{ K}$  above. We isolated the magnetic scattering from instrumental background and nuclear scattering contributions by subtracting the high temperature dataset from the low temperature dataset (Fig. 4c), which allowed us to identify the magnetic Bragg peaks. We were able to index these reflections with a propagation vector  $\mathbf{k} = \frac{1}{2}00$  and using symmetry-mode analysis in the ISODISTORT software suite<sup>39</sup> we identified there were two possible irreducible representations (irreps),  $mY_1^-$  and  $mY_2^-$  in Miller and Love’s notation.<sup>40</sup> After calibration of the nuclear scale factor through Rietveld refinement of nuclear structure against the high temperature dataset, we carried out Rietveld refinement of the magnetic structure using each irrep against the temperature subtracted dataset. We found for both nuclear and magnetic

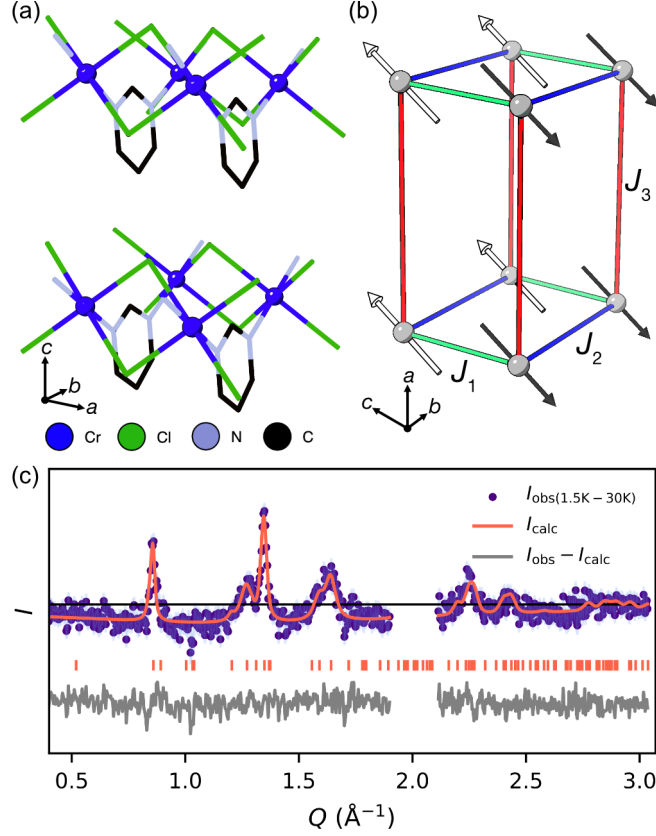


Figure 4: (a) The crystal structure of  $\text{CrCl}_2(\text{pym})$ , nuclear axes shown. (b) The magnetic structure, highlighting the three most important exchange interactions,  $J_n$ , magnetic axes shown. (c) Rietveld refinement of temperature subtracted neutron scattering data. Data between  $Q = 1.9 \text{ \AA}^{-1}$  and  $2.1 \text{ \AA}^{-1}$  were excluded from the refinement due to incomplete subtraction of nuclear Bragg peaks due to thermal expansion.

refinement that a  $hkl$ -dependent peak broadening term was necessary to account for the variation in measured peak widths. This showed that only the  $mY_1^-$  irrep was consistent with experimental data (Fig. 4c). The  $mY_1^-$  irrep lowers the symmetry of the structure to  $P_c2_1/c$  with the magnetic unit cell relating to the nuclear cell as follows:  $a_{\text{mag.}} = c_{\text{nuc.}}$ ,  $b_{\text{mag.}} = b_{\text{nuc.}}$  and  $c_{\text{mag.}} = 2a_{\text{nuc.}}$  (Fig. 4a & b).

The magnetic structure derived from this refinement is a collinear structure consisting of antiferromagnetically correlated  $\text{CrCl}_2$  spin chains ferromagnetically correlated through the pym ligands, with interlayer ferromagnetic correlations (Fig. 4b). The refined magnetic moment was Cr was determined to be  $M_0 = 2.61(7)\mu_B$ , significantly less than the spin-only value of  $M = gS = 4\mu_B$ .



The magnetic moments in our model lie within the *ac*-plane, however components along the *b*-direction would be permitted by symmetry. The presence of a component along *b* would result in intensity at the  $011_{\text{mag}}$  peak position ( $Q = 1.00 \text{ \AA}^{-1}$ ) which is not seen in our data and so any non-collinearity must be small,  $\theta < 8^\circ$ . The background of this subtracted  $I_{1.5\text{K}} - I_{30\text{K}}$  dataset contains a broad negative feature characteristic of magnetic diffuse scattering, which could be modelled by a broad Lorentzian peak centred at the  $101_{\text{mag}}$  peak position, with an isotropic correlation length at 30 K  $\lambda = 2.8(2) \text{ \AA}$ .

## Inelastic neutron scattering

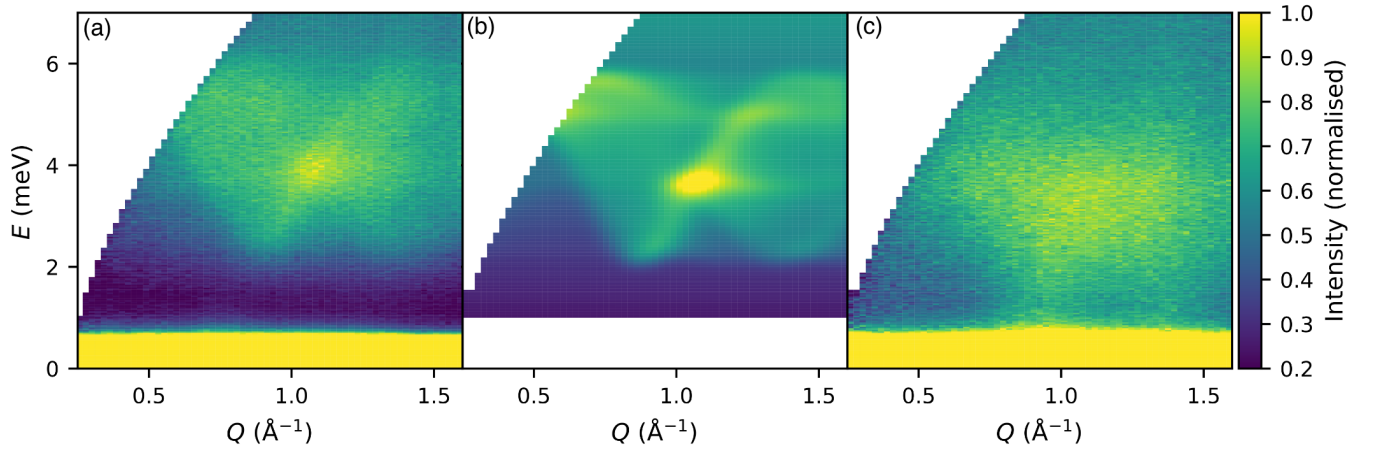


Figure 5: Time-of-flight powder INS spectra of  $\text{CrCl}_2(\text{pym})$  with  $E_i = 12.14 \text{ meV}$  measured at (a) 1.7 K and (c) 25 K. (b) LSWT calculated scattering intensity fitted to the 1.7 K data, with parameters  $J_1 = -1.13(4)$ ,  $J_2 = 0.10(2)$ ,  $J_3 = 0.01(1)$  and  $D = -0.11(1) \text{ meV}$ . Hamiltonian described in Eqn. 1.

To measure the parameters of the magnetic Hamiltonian and search for signatures of low-dimensional magnetism, we collected INS spectra on the same powder sample of  $\text{CrCl}_2(\text{pym})$  at 1.7 and 25 K using the LET spectrometer at ISIS, using rep-rate multiplication to measure at multiple  $E_i$  simultaneously ( $E_i = 12.14, 3.70, 1.77 \text{ meV}$ ). The spectra collected at 1.7 K show a clear excitation centred at  $\Delta E = 4.1(2) \text{ meV}$  with an energy gap of  $2.2(1) \text{ meV}$  (Fig. 5a) despite the presence of an elevated background due to the incoherent  $^1\text{H}$  scattering. The intensity of this feature rapidly falls with increasing  $Q$ , until it is masked by phonons,

indicating this excitation is magnetic in origin. We were able to quantitatively fit these data using linear spin wave theory (LSWT) (Fig. 5b) as implemented by the SpinW software package,<sup>41</sup> using the following magnetic Hamiltonian,

$$\mathcal{H} = \sum_{\langle ij \rangle} -J_{ij} \mathbf{S}_i \cdot \mathbf{S}_j + \sum_i D(S_i^z)^2, \quad (1)$$

comprising Heisenberg exchange,  $J_{ij}$ , for the three nearest neighbours (*i.e.* along the  $\text{CrCl}_2$  through the pym ligand and between layers) and a single ion anisotropy,  $D$  (Fig. 4b). We began by estimating the approximate values for each of  $J_1$ ,  $J_2$ ,  $J_3$  and  $D$  using our bulk magnetic measurements and extrapolating from analogous compounds.<sup>26</sup> These initial parameters were then optimised using least square requirements of the calculated spectrum, including a refined multiplicative scale factor and a background linear in both  $Q$  and  $\Delta E$ , against the experiment data which gave  $J_1 = -1.13(4)$  meV,  $J_2 = 0.10(2)$  meV,  $0 < J_3 < 0.01(1)$  meV and  $D = -0.15(3)$  meV. The value of  $D$  was corrected for kinematical consistency<sup>42</sup>, as by default SpinW uses the inconsistent  $D' = D[1 - \frac{1}{2S}] = \frac{3}{4}D$ . A grid search was undertaken to confirm this as a unique solution. Our experimental spectra were consistent with a negligible value for  $J_3$ , however the ground state determined by PND indicates that  $J_3$  must be ferromagnetic. The ratio of  $J_1/J_2 = 11(2)$  indicates that the magnetic interactions in this materials are primarily one-dimensional. We therefore decided to investigate the spectrum of  $\text{CrCl}_2(\text{pym})$  in the short-range ordered regime to search for coherent excitations (Fig. 5c). Energy cuts, integrated over momentum transfer,  $0.76 < Q < 1.84 \text{ \AA}^{-1}$ , showed no clear evidence of a gap in the paramagnetic regime, for both  $E_i = 12.14$  meV and  $E_i = 3.70$  meV, suggesting this material is not within the Haldane phase (Fig. S3b), although the comparatively high temperature compared to the expected gap size,  $T/\Delta = 25$  will make this challenging.

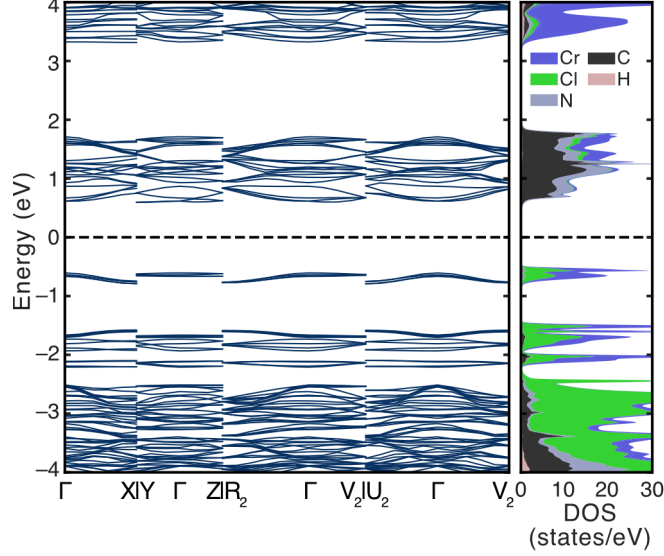


Figure 6: Electronic band structure and projected density of states of the  $2 \times 2 \times 1$  supercell using CASTEP and the PBE+U+MBD\* ( $U_{\text{eff}} = 3$  eV) functional. The energy zero has been set at the Fermi energy and is shown by the dashed line. The projected density of states has been decomposed by element.

## Density-functional theory

To understand the origin of the observed low-dimensional interactions we carried out collinear spin-polarized plane-wave density-functional theory (DFT) calculations, by exploring the electronic structure of the DFT ground-state spin configuration and calculating the exchange energies using the broken symmetry approach.<sup>43</sup> We first optimised the geometry of the experimental structure using the PBE functional along with a many-body semi-empirical dispersion correction (MBD\*)<sup>44</sup> to describe the weak van der Waals forces between the layers.<sup>45</sup> We found that this structure was both too dense, with a unit-cell volume of  $297.68 \text{ \AA}^3$ , 4.8% smaller than experimental value of  $312.75 \text{ \AA}^3$ , and lacked the JT distortion characteristic of Cr(II). We therefore included an effective Coulomb on-site energy,  $U_{\text{eff}} = U - J$  where  $U$  is the on-site repulsion and  $J$  the exchange energy, to account for the overly delocalised Cr d-states. A range of values for  $U_{\text{eff}}$  have been previously explored for Cr, from  $U_{\text{eff}} = 2.1$  eV to  $U_{\text{eff}} = 3.5$  eV.<sup>46,47</sup> We found that  $U_{\text{eff}} = 3$  eV was able to accurately capture the physics of this system, and produced a structure with both a JT distortion and, as a bonus, a volume

within +0.2% of experiment.

Exchange interactions were calculated using a  $2 \times 2 \times 1$  supercell of the optimised structure (*i.e.* containing eight distinct Cr atoms) decorated with eight distinct magnetic orderings. Single point energy calculations were then carried out on each configurations, and these DFT+ $U$  total energies were then fitted to the Hamiltonian described in Eqn. 1 with  $D = 0$ , *i.e.* the Heisenberg limit. We carried out these calculations using a series of values of  $U_{\text{eff}}$  to ensure consistency of behaviour (Fig. S10). For our optimised value of  $U_{\text{eff}} = 3$  eV, we obtained a self-consistent set of superexchange interactions of  $J_1 = -2.53(5)$  meV,  $J_2 = 0.30(5)$  meV,  $J_3 = -0.09(5)$  meV. To test the robustness of our DFT+ $U$  calculations, we performed hybrid calculations using fraction of Fock exchange as implemented in the HSE functional<sup>48-50</sup> while maintaining a  $U_{\text{eff}} = 3$  eV. HSE calculations are computationally expensive due to the calculation of Fock exchange and require the use of norm-conserving pseudopotentials within CASTEP, which limited the sampling of the Brillouin zone and our ability to explore geometry optimisations. Nevertheless, we found that using the HSE functional comparable exchange interactions  $J_1 = -2.39(1)$  meV,  $J_2 = 0.46(1)$  meV,  $J_3 = -0.15(1)$  meV. These energies are comparable in magnitude to those found experimentally for  $\text{CrCl}_2(\text{pym})$ , but are notably larger, likely due to the unphysically large degree of delocalisation.

Our calculations not only allow us to predict the interaction energies, but also to explore the electronic structure of this material (Fig. 6). The predicted thermal band gap is approximately 1.2 eV, and the projection of the DOS onto local orbitals shows that the top of the valence band is broadly Cr and Cl based, whilst the organic linker pym states are the bottom of the conduction band. This can also be observed in the frontier orbitals, where the HOMO resembles the Cr  $d_{z^2}$  orbital antibonding with Cl  $p$  orbitals and the LUMO is an antibonding  $\pi$  molecular orbital with a single additional node, suggesting that the lowest lying excitations will be of MLCT character. The spin density is predominantly around the Cr, however, there is significant density on both Cl and pym ligands (Fig. 7). Notably, the

spin density on pym appears to be primarily of  $\pi$  character, and alternates in sign round the ring (Fig. 7b).

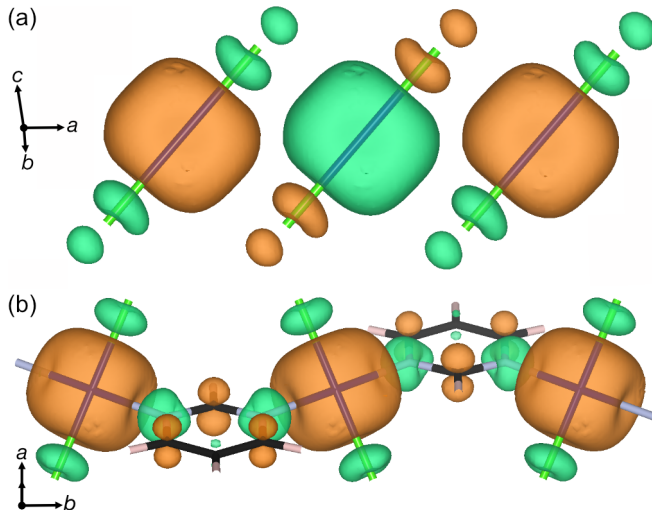


Figure 7: Spin density isosurfaces ( $0.015 \text{ e } \text{\AA}^{-3}$ ) highlighting the (a) the Cr-Cl chain and (b) the Cr-pym chain, derived from our CASTEP PBE+U+MBD\* ( $U_{\text{eff}} = 3 \text{ eV}$ ) and c2x calculations.<sup>51</sup>

## Discussion

Metal N-heterocycle dihalides are a diverse family of MOMs and our study of  $\text{CrCl}_2(\text{pym})$  provides one of the most in-depth investigations of the magnetic properties of these materials. There are two common compositions:  $\text{MX}_2\text{L}_2$  and  $\text{MX}_2\text{L}$ . The monoligand analogues usually contain linear  $\text{MX}_2$  chains, and therefore tend to show primarily 1D magnetic behaviour, *e.g.*  $\text{NiCl}_2(\text{pyrazine})$  consists of ferromagnetic  $\text{NiCl}_2$  chains antiferromagnetically coupled with  $T_N = 10.2 \text{ K}$ ,<sup>3</sup>  $\text{CuCl}_2(\text{pyrazine})$  is also a very good example of a 1D magnet with no order reported down to  $1.8 \text{ K}$ , but the strongest interaction in fact occurs through Cu—pyrazine—Cu bridges ( $J = -28 \text{ K}$ ), due to the JT distortion suppressing exchange in the  $\text{CuCl}_2$  chain.<sup>52</sup> Preliminary studies of the magnetism of pyrimidine analogues,  $\text{MCl}_2(\text{pym})$   $\text{M} = \text{Mn}, \text{Co}, \text{Cu}$ , also detect no magnetic order down to  $1.8 \text{ K}$  although there are weak AFM interactions present.<sup>32</sup> The strong interactions, particularly occurring through the

CrCl<sub>2</sub> chain, and magnetic order found in CrCl<sub>2</sub>(pym) are therefore in striking contrast. Additionally, the ferromagnetic exchange we observe occurring through the pym ligand is relatively uncommon for molecular ligands, for example, antiferromagnetic interactions are the norm for pyrazine-bridged MOMs.<sup>53–59</sup> This ferromagnetic exchange has been previously observed in pym-bridged MOMs, *e.g.* M(NCS)<sub>2</sub>(pym)<sub>2</sub> ( $M = \text{Ni}$  and  $\text{Co}$ ),<sup>60–62</sup> and has been rationalised by a three-atom  $\pi$ -pathway. Our DFT calculations give further credence to the importance of this pathway.

The bispyrimidine metal chlorides, MCl<sub>2</sub>(pym)<sub>2</sub>  $M = \text{Fe}$ ,  $\text{Co}$ ,  $\text{Ni}$  and MBr<sub>2</sub>(pym)<sub>2</sub>  $M = \text{Co}$ , unlike most materials in this family adopt 3D chiral diamondoid structures.<sup>33–35</sup> MCl<sub>2</sub>(pym) all magnetically order with canted AFM structures,  $T_N = 7.4$  K, 4.7 K and 16.3 K for  $M = \text{Fe}$ ,  $\text{Co}$  and  $\text{Ni}$  respectively, likely arising from the interplay between the superexchange interactions and the significant single-ion anisotropy, the principal axes of which are non-collinear.<sup>33</sup> Bulk susceptibility studies have shown enhancement of  $T_N$  at moderate pressure ( $\Delta T_N/T_N = 15\%$  at 0.7 GPa),<sup>35</sup> which suggests that high pressure investigations of Cr-based MOMs may also uncover pressure-switchable magnetic functionality.<sup>63</sup>

The presence of a JT distortion is strong evidence of Cr<sup>2+</sup>, which stands in contrast to the related CrCl<sub>2</sub>(pyrazine)<sub>2</sub>, in which Cr<sup>2+</sup> spontaneously reduces the ligated pyrazine to a radical anion, and thereby dramatically enhancing its conductivity and magnetic superexchange.<sup>8</sup> The sensitivity of this metal-ligand redox to the coordination sphere is shown by Cr(OSO<sub>2</sub>CH<sub>3</sub>)<sub>2</sub>(pyrazine)<sub>2</sub>, in which Cr remains as Cr<sup>2+</sup> with a JT distortion.<sup>56</sup> Studies of molecular complexes have shown this non-innocent behaviour is favoured by a strong ligand-field environment and a low energy ligand LUMO,<sup>64</sup> and is consistent with the observed innocence of CrCl<sub>2</sub>(pym), which has both weaker ligand field than CrCl<sub>2</sub>(pyz)<sub>2</sub> and a higher energy ligand LUMO (pyrazine,  $E_{\text{red}} = +1.10$  V and pym  $E_{\text{red}} = +0.84$  V vs. Li/Li<sup>+</sup>).<sup>65</sup>

Our data clearly show that CrCl<sub>2</sub>(pym) has a conventional Néel AFM ground state,  $T_N = 20.0(3)$  K, but also that there is significant magnetic low-dimensionality above  $T_N$ .

The frustration parameter,  $f = \frac{|\theta_{\text{CW}}|}{T_N} = 2.7$ , derived from bulk property measurements

hints at suppression of magnetic order. As the magnetic lattice does not show an obvious mechanism for geometric frustration, this is likely due to a combination of single-ion anisotropy and low-dimensionality arising from the large differences in strength of superexchange in different crystallographic directions.

Additionally, the presence of magnetic diffuse scattering at 30 K not present at 1.5 K, indicates the presence of short-range magnetic correlations retained above  $T_N$ . Finally, our analysis of the INS spectra show that the AFM superexchange through the Cr–Cl–Cr bridge is an order of magnitude larger than all other superexchange interactions,  $|\frac{J_1}{J_2}| = 11(2)$ .

The importance of low-dimensionality can also be seen in the reduction in the apparent size of the  $\text{Cr}^{2+}$  ordered moment determined via neutron diffraction. The low-dimensionality of the structure can reduce the refined moment through disorder, both static short-chain defects and stacking faults<sup>66,67</sup> and dynamic zero-point fluctuations<sup>68</sup>. Additionally, as is common in many metal organic magnets,<sup>69</sup> there is appreciable delocalisation of the spin-density onto the ligands, which Mulliken analysis of the DFT-derived electron density suggests is approximately 10%. These factors in combination explain the substantial reduction in the ordered moment (approximately one-third) from that expected moment size, though it is challenging to evaluate their relative contributions.

Despite this low-dimensionality, our data indicate that like other  $S = 2$  candidate AFM chains,  $\text{CrCl}_2(\text{pym})$  does not show clear Haldane physics. The presence of long range order at  $T_N/J_1 = 1.5$  hinders observations at low temperatures and the non-negligible single ion anisotropy ( $D = -0.15(3)$  meV,  $D/J_1 = 0.13(2)$ ) is sufficient to suppress the Haldane phase, for which the critical value is predicted to be  $D/J_1 = 0.04$ .<sup>25</sup>  $\text{CrCl}_2(\text{pym})$  is therefore comparable to the other identified candidate  $S = 2$  spin chains in both of these parameters,<sup>28–30</sup> including  $\text{CrCl}_2$ ,<sup>26</sup>  $\text{MnCl}_3(\text{bipy})$ <sup>27,70</sup> and  $\text{CsCrCl}_3$ ,<sup>71</sup> but none have shown clear evidence of a gapped inelastic neutron spectrum in the disordered phase.

The compound  $\text{CrCl}_2(\text{pym})$  is most similar to, both structurally and magnetically, is  $\text{CrCl}_2$ ,<sup>26</sup> which also has quasi-1D antiferromagnetic  $\text{CrCl}_2$  chains formed from edge-sharing

octahedra ( $J_1 = -1.13(13)$  meV,  $D' = -0.11(2)$  meV). However, closer examination reveals significant structural differences that make these magnetic similarities quite surprising. In  $\text{CrCl}_2(\text{pym})$  the JT distortion means every superexchange pathway within the  $\text{CrCl}_2$  spin chain passes through a significantly lengthened bond, whereas in  $\text{CrCl}_2$  the equivalent JT distortion lies out of the spin-chain plane and so all Cr–Cl bonds in the chain are short. Superexchange through a JT-lengthened pathway is ordinarily weak, as is indeed found for the direction perpendicular to the  $\text{CrCl}_2$  spin chain in inorganic  $\text{CrCl}_2$ , with an order of magnitude weaker exchange  $J_2 = -0.12(7)$  meV.

A second distinction between these two compounds is the potential for tuning the interactions through substitution of the ligands. Replacing pyrimidine by a larger bridging ligand may reduce inter-chain exchange, suppressing long-range order and allowing access to the paramagnetic  $S = 2$  quasi-1D AFM at lower temperatures. For example, in  $\text{NiCl}_2\text{L}$  substituting pyrazine for 1,2-bis(4-pyridyl)ethane reduces  $T_N$  from 10.2 K to 5.6 K.<sup>3</sup> Equally, optimisation of the octahedral coordination environment can minimise  $D$ , for example in a family of closely related  $\text{Ni}^{2+}$  compounds, matching of the ligand field strengths reduces the size of the easy-plane anisotropy by a factor of 4.<sup>72</sup> Our measurements of the INS data already suggest that the interlayer interactions are not significant, but delamination of these van der Waals sheets, as demonstrated for other magnetic metal-organic nanosheets,<sup>73</sup> may provide an alternative route to better magnetic isolation. These results suggest therefore that bridging  $\text{CrCl}_2$  spin chains with organic ligands may provide promising future candidates for  $S = 2$  Haldane chains.

## Conclusion

We have reported the crystal structure, bulk magnetic properties, magnetic ground state and magnetic excitations of a new coordination polymer,  $\text{CrCl}_2(\text{pym})$ . We have shown that the oxidation state of chromium in this compound is  $\text{Cr}^{2+}$ , remaining  $S = 2$ , unlike related



CrCl<sub>2</sub> derived MOMs which undergo redox to form triplet Cr<sup>3+</sup>-radical ligand pairs.<sup>8,64</sup> CrCl<sub>2</sub>(pym) is found to be a  $S = 2$  quasi-one-dimensional antiferromagnet, with an order of magnitude separation in energy scales of superexchange,  $|J_1/J_2| = 11(2)$ . However we did not find clear evidence of the Haldane gap in the disordered phase, suggesting the small  $J_2$  and  $D$  are sufficient in this compound to either suppress the  $S = 2$  Haldane phase or mask it through the stabilisation of long range order. The proximity of CrCl<sub>2</sub>(pym) to the Haldane region of the phase diagram, and the modularity inherent to MOMs suggest that optimising the magnetic properties of these systems, including both superexchange<sup>3</sup> and single-ion-anisotropy,<sup>72</sup> is a new and promising route to the  $S = 2$  Haldane phase.

## Experimental

### Synthesis

Synthesis and handling of CrCl<sub>2</sub>(pym) was performed in a dry Ar or N<sub>2</sub> atmosphere using a MBraun LABstar glovebox or Schlenk line. The reaction of CrCl<sub>2</sub> (200 mg, 1.63 mmol; Fisher Scientific, 99.9%) and pyrimidine (500 mg, 6.24 mmol; Sigma-Aldrich,  $\geq 98.0\%$ ) in 50 mL methanol (MeOH) rapidly precipitates an orange-brown microcrystalline powder. The CrCl<sub>2</sub>(pym) product was then dried *in vacuo* giving a ca. 90% total yield. The measured (calculated) elemental composition was: C, 23.45% (23.67%); H, 1.99% (2.40%); N, 12.94% (13.80%). This procedure, with quantities scaled up (CrCl<sub>2</sub>, 3.0 g; pyrimidine, 4.0 g; MeOH, 300 mL), was used to synthesise the sample used for neutron-scattering measurements. Crystals of sufficient size for X-ray diffraction studies ( $127 \times 46 \times 26 \mu\text{m}$ ) were grown by vapour diffusion of pyrimidine (100 mg, 1.25 mmol) into a concentrated solution of CrCl<sub>2</sub> in 1 mL MeOH (10 mg, 0.08 mmol).

## Powder X-ray diffraction

PXRD data were collected using a PANalytical X’Pert Pro diffractometer equipped with monochromated Cu  $K\alpha_1$  radiation ( $\lambda = 1.5406 \text{ \AA}$ ). The tube voltage and current were 40 kV and 40 mA, respectively. Scans were performed from  $2^\circ$  to  $60^\circ$  on a zero background silicon crystal plate. Peak fitting, Pawley and Rietveld refinement were performed using Topas Academic v6.<sup>74</sup>

## Single crystal X-ray diffraction

A diffraction-quality single crystal of  $\text{CrCl}_2(\text{pym})$  was mounted on a polymer-tipped MiTe-Gen MicroMount<sup>TM</sup> using Fomblin (YR-1800 perfluoropolyether oil). The sample was cooled rapidly to 120 K in a stream of cold  $\text{N}_2$  gas, using a Oxford Cryosystems open flow cryostat. Diffraction data were collected on an Oxford Diffraction GV1000 (AtlasS2 CCD area detector, mirror-monochromated Cu- $K\alpha$  radiation source;  $\lambda = 1.54184 \text{ \AA}$ ,  $\omega$  scans). Cell parameters were refined from the observed positions of all strong reflections and absorption corrections were applied using a Gaussian numerical method with beam profile correction (CrysAlisPro). The structure was solved and refined in Olex2<sup>75</sup> using SHELXT<sup>76</sup> and SHELXL<sup>77</sup>, respectively.

## Magnetic susceptibility

Magnetic property measurements were carried out on a Quantum Design MPMS superconducting quantum interference device (SQUID). A polycrystalline sample of  $\text{CrCl}_2(\text{pym})$  (26.6 mg) was immobilised in eicosane (44.5 mg) and sealed in a low-paramagnetic-impurity borosilicate glass ampoule under vacuum. Magnetic susceptibility measurements were performed under field cooled (FC) and zero-field cooled (ZFC) conditions in a 0.01 T *dc* field from 2 K to 300 K. Isothermal magnetisation measurements were performed at 2 K from 0 T to 5 T to  $-5 \text{ T}$  to 0 T. Data were corrected for the diamagnetism of the sample using

Pascal’s constants.<sup>78</sup>

## Heat capacity

Heat-capacity measurements were carried out on a 4.2 mg pellet of  $\text{CrCl}_2(\text{pym})$  and silver powder (50 wt. %), using a Quantum Design Dynacool Physical Property Measurement system (PPMS), between 2 and 60 K. Apiezon N grease was used to ensure good thermal contact. Contributions to the heat capacity due to Apiezon N were measured separately and subtracted, contributions due to silver were subtracted using tabulated values.<sup>79</sup>

## Powder neutron diffraction

PND measurements were carried out on the D1B neutron diffractometer at Institut Laue-Langevin, Grenoble, France. Measurements were collected at 1.5 K and 30 K with  $\lambda = 2.52$  Å between  $0.77^\circ$  and  $128.67^\circ$  with steps of  $0.1^\circ$ . The nuclear structure determined from single crystal X-ray diffraction was Rietveld refined against neutron diffraction data to evaluate phase purity. Due to the low intensity of magnetic reflections, the magnetic structure was determined by refinement against data from which background and nuclear Bragg peaks were removed by subtraction of data collected at 30 K from those collected at 1.5 K. The magnetic Bragg peaks were indexed to determine the magnetic propagation vector and then the allowed magnetic irreducible representations were determined using symmetry-mode analysis on the ISODISTORT software.<sup>39</sup> Using the scale factor determined from Rietveld refinement of the nuclear structure against data at 30 K, and peak parameters determined from Pawley refinement of the nuclear structure against data at 30 K, the direction and magnitude of the ordered moment for the subtracted dataset were refined using TOPAS-ACADEMIC 6.0.<sup>74</sup>

## Inelastic neutron scattering

Inelastic neutron scattering (INS) measurements were performed on the LET time-of-flight direct geometry spectrometer at ISIS.<sup>80</sup> The sample (4 g) was contained in a thin aluminum can of diameter 15 mm and height 45 mm and cooled in a helium cryostat. The data were collected at 1.7 K and 25 K, for 10 h and 7 h respectively, with  $E_i = 12.14$  meV using the rep-rate multiplication method.<sup>81,82</sup> The data were reduced using the Mantid-Plot software package.<sup>83</sup> The raw data were corrected for detector efficiency and time independent background following standard procedures.<sup>84</sup>

## Density-functional theory

Plane-wave density-functional theory calculations were performed using version 19.1 of the CASTEP code.<sup>85</sup> The Brillouin zone was integrated using a Monkhorst-Pack grid of  $k$ -points, finer than  $2\pi \times 0.05 \text{ \AA}^{-1}$  spacing.<sup>86</sup> A Gaussian smearing scheme with a smearing width of 0.20 eV was used during the electronic minimisation process. Vanderbilt ultrasoft pseudopotentials were used for computational efficiency (Tab. S3).<sup>87</sup> The basis set included plane-waves up to an associated kinetic energy of 1100 eV. Geometry optimisations converged until resultant forces were less than 0.05 eV/ $\text{\AA}$ . The OptaDOS post-processing code was used to integrate individual Kohn-Sham eigenvalues into an electronic density of states,<sup>88</sup> and the Matador high-throughput environment was used to obtain electronic band structure and density of states plots.<sup>89</sup>

## Supporting Information

Information on single-crystal and powder X-ray diffraction, additional inelastic neutron scattering data, powder X-ray and neutron diffraction data, isothermal magnetisation measurements, magnetic susceptibility analysis, X-ray photoelectron spectroscopy, transmission electron micrographs and additional details of DFT calculations (PDF).

CCDC 2213061, crystallographic data (CIF).

Magnetic structure (mCIF).

Additional research data for this Article may be accessed at no charge and under CC-BY license at the University of Nottingham Research Data Management Repository <https://doi.org/10.17639/n>

Inelastic neutron scattering data measured at ISIS Neutron and Muon Source is available at <https://doi.org/10.5286/ISIS.E.RB2090119>.

CCDC 2213061 contains the supplementary crystallographic data for this paper. These data can be obtained free of charge via [www.ccdc.cam.ac.uk/data\\_request/cif](http://www.ccdc.cam.ac.uk/data_request/cif), or by emailing [data\\_request@ccdc.cam.ac.uk](mailto:data_request@ccdc.cam.ac.uk), or by contacting The Cambridge Crystallographic Data Centre, 12 Union Road, Cambridge CB2 1EZ, U.K.; fax: + 44 1223 336033.

## TOC

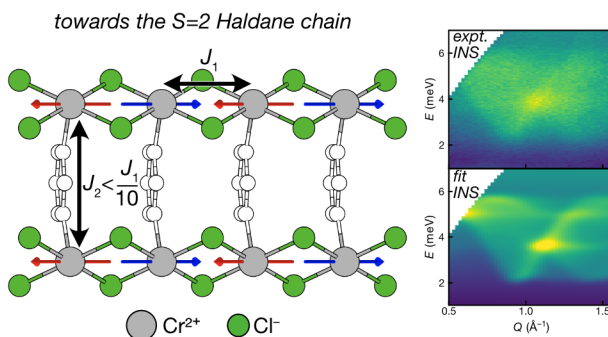


Figure 8: TOC Figure

## Acknowledgement

J.P. and M.J.C. acknowledge the School of Chemistry, University of Nottingham for support from the Hobday bequest. A.J.M. acknowledges funding from EPSRC (EP/P003532/1). The authors acknowledge networking support via the EPSRC Collaborative Computational Projects, CCP9 (EP/M022595/1) and CCP-NC (EP/T026642/1). Computing resources

were provided by the Sulis HPC service (EP/T022108/1). We acknowledge the ILL for beamtime under proposal EASY-778. We acknowledge ISIS for beamtime under proposal RB2090119. J.P. acknowledges Jesum Alves Fernandes for training and assistance with XPS analysis. J.P. acknowledges Benjamin Weare for TEM analysis. Heat Capacity measurements were performed using the Advanced Materials Characterisation Suite, funded by EP-SRC Strategic Equipment Grant EP/M000524/1. J.P. and M.J.C. acknowledge Siân Dutton and Joseph Paddison for useful discussions.

## References

- (1) Thorarinsdottir, A. E.; Harris, T. D. Metal–Organic Framework Magnets. *Chemical Reviews* **2020**, *120*, 8716–8789.
- (2) Zhao, D.; Timmons, D. J.; Yuan, D.; Zhou, H.-C. Tuning the Topology and Functionality of Metal-Organic Frameworks by Ligand Design. *Accounts of Chemical Research* **2011**, *44*, 123–133.
- (3) Cortijo, M.; Herrero, S.; Jiménez-Aparicio, R.; Matesanz, E. Modulation of the Magnetic Properties of Two-Dimensional Compounds [NiX<sub>2</sub>(N–N)] by Tailoring Their Crystal Structure. *Inorganic Chemistry* **2013**, *52*, 7087–7093.
- (4) Canepa, P.; Chabal, Y. J.; Thonhauser, T. When Metal Organic Frameworks Turn into Linear Magnets. *Physical Review B* **2013**, *87*, 094407.
- (5) Harcombe, D. R.; Welch, P. G.; Manuel, P.; Saines, P. J.; Goodwin, A. L. One-Dimensional Magnetic Order in the Metal-Organic Framework Tb(HCOO)<sub>3</sub>. *Physical Review B* **2016**, *94*, 174429.
- (6) Vasiliev, A.; Volkova, O.; Zvereva, E.; Markina, M. Milestones of Low-D Quantum Magnetism. *npj Quantum Materials* **2018**, *3*, 1–13.

- (7) Ziebel, M. E.; Darago, L. E.; Long, J. R. Control of Electronic Structure and Conductivity in Two-Dimensional Metal–Semiquinoid Frameworks of Titanium, Vanadium, and Chromium. *Journal of the American Chemical Society* **2018**, *140*, 3040–3051.
- (8) Pedersen, K. S. et al. Formation of the Layered Conductive Magnet  $\text{CrCl}_2(\text{Pyrazine})_2$  through Redox-Active Coordination Chemistry. *Nature Chemistry* **2018**, *10*, 1056–1061.
- (9) Perlepe, P. et al. Metal–Organic Magnets with Large Coercivity and Ordering Temperatures up to 242°C. *Science* **2020**, *370*, 587–592.
- (10) Murphy, R. A.; Darago, L. E.; Ziebel, M. E.; Peterson, E. A.; Zaia, E. W.; Mara, M. W.; Lussier, D.; Velasquez, E. O.; Shuh, D. K.; Urban, J. J.; Neaton, J. B.; Long, J. R. Exchange Bias in a Layered Metal–Organic Topological Spin Glass. *ACS Central Science* **2021**, *7*, 1317–1326.
- (11) Park, J. G.; Collins, B. A.; Darago, L. E.; Runčevski, T.; Ziebel, M. E.; Aubrey, M. L.; Jiang, H. Z. H.; Velasquez, E.; Green, M. A.; Goodpaster, J. D.; Long, J. R. Magnetic Ordering through Itinerant Ferromagnetism in a Metal–Organic Framework. *Nature Chemistry* **2021**, *13*, 594–598.
- (12) Yamada, M. G.; Fujita, H.; Oshikawa, M. Designing Kitaev Spin Liquids in Metal–Organic Frameworks. *Physical Review Letters* **2017**, *119*, 057202.
- (13) Huang, X.; Zhang, S.; Liu, L.; Yu, L.; Chen, G.; Xu, W.; Zhu, D. Superconductivity in a Copper(II)-Based Coordination Polymer with Perfect Kagome Structure. *Angewandte Chemie International Edition* **2018**, *57*, 146–150.
- (14) Coronado, E. Molecular Magnetism: From Chemical Design to Spin Control in Molecules, Materials and Devices. *Nature Reviews Materials* **2020**, *5*, 87–104.

- (15) Dender, D. C.; Hammar, P. R.; Reich, D. H.; Broholm, C.; Aeppli, G. Direct Observation of Field-Induced Incommensurate Fluctuations in a One-Dimensional  $S = 1/2$  Antiferromagnet. *Physical Review Letters* **1997**, *79*, 1750–1753.
- (16) Zvyagin, S. A.; Kolezhuk, A. K.; Krzystek, J.; Feyerherm, R. Excitation Hierarchy of the Quantum Sine-Gordon Spin Chain in a Strong Magnetic Field. *Physical Review Letters* **2004**, *93*, 027201.
- (17) Liu, J.; Kittaka, S.; Johnson, R. D.; Lancaster, T.; Singleton, J.; Sakakibara, T.; Kohama, Y.; van Tol, J.; Ardavan, A.; Williams, B. H.; Blundell, S. J.; Manson, Z. E.; Manson, J. L.; Goddard, P. A. Unconventional Field-Induced Spin Gap in an  $S = 1/2$  Chiral Staggered Chain. *Physical Review Letters* **2019**, *122*, 057207.
- (18) Renard, J. P.; Verdaguer, M.; Regnault, L. P.; Erkelens, W. A. C.; Rossat-Mignod, J.; Stirling, W. G. Presumption for a Quantum Energy Gap in the Quasi-One-Dimensional  $S = 1$  Heisenberg Antiferromagnet  $\text{Ni}(\text{C}_2\text{H}_8\text{N}_2)_2\text{NO}_2(\text{ClO}_4)$ . *Europhysics Letters (EPL)* **1987**, *3*, 945–952.
- (19) Haldane, F. D. M. Nonlinear Field Theory of Large-Spin Heisenberg Antiferromagnets: Semiclassically Quantized Solitons of the One-Dimensional Easy-Axis Néel State. *Physical Review Letters* **1983**, *50*, 1153–1156.
- (20) Haldane, F. D. M. Continuum Dynamics of the 1-D Heisenberg Antiferromagnet: Identification with the  $O(3)$  Nonlinear Sigma Model. *Physics Letters A* **1983**, *93*, 464–468.
- (21) Mutka, H.; Soubeyroux, J. L.; Bourleaux, G.; Colombet, P. Support for the Haldane Conjecture: Gap for Magnetic Excitations in the Quasi-One-Dimensional  $S=1$  Heisenberg Antiferromagnet  $\text{AgVP}_2\text{S}_6$ . *Physical Review B* **1989**, *39*, 4820–4823.
- (22) Takeuchi, T.; Hori, H.; Yosida, T.; Yamagishi, A.; Katsumata, K.; Renard, J.-P.; Gadet, V.; Verdaguer, M.; Date, M. Magnetization Process of Haldane Materials TMNIN and NINAZ. *Journal of the Physical Society of Japan* **1992**, *61*, 3262–3266.



- (23) Landee, C. P.; Reza, K. A.; Bond, M. R.; Willett, R. D. Low-Temperature Crystal Structures of Two Haldane-gap Nickel Chains, NENP and NENF. *Physical Review B* **1997**, *56*, 147–153.
- (24) Williams, R. C. et al. Near-Ideal Molecule-Based Haldane Spin Chain. *Physical Review Research* **2020**, *2*, 013082.
- (25) Schollwöck, U.; Jolicoeur, T. Haldane Gap and Hidden Order in the  $S = 2$  Antiferromagnetic Quantum Spin Chain. *Europhysics Letters (EPL)* **1995**, *30*, 493–498.
- (26) Stone, M. B.; Ehlers, G.; Granroth, G. E.  $S = 2$  Quasi-One-Dimensional Spin Waves in  $\text{CrCl}_2$ . *Physical Review B* **2013**, *88*, 104413.
- (27) Granroth, G.; Nagler, S.; Coldea, R.; Eccleston, R.; Ward, B.; Talham, D.; Meisel, M. Neutron-Scattering Studies of the  $S = 2$  Antiferromagnetic Chain  $\text{MnCl}_3(\text{C}_{10}\text{D}_8\text{N}_2)$ . *Applied Physics A: Materials Science & Processing* **2002**, *74*, s868–s870.
- (28) Léone, P.; André, G.; Doussier, C.; Moëlo, Y. Neutron Diffraction Study of the Magnetic Ordering of Jamesonite ( $\text{FePb}_4\text{Sb}_6\text{S}_{14}$ ). *Journal of Magnetism and Magnetic Materials* **2004**, *284*, 92–96.
- (29) Stock, C.; Chapon, L. C.; Adamopoulos, O.; Lappas, A.; Giot, M.; Taylor, J. W.; Green, M. A.; Brown, C. M.; Radaelli, P. G. One-Dimensional Magnetic Fluctuations in the Spin-2 Triangular Lattice  $\alpha\text{-NaMnO}_2$ . *Physical Review Letters* **2009**, *103*, 077202.
- (30) Birk, T.; Pedersen, K. S.; Piligkos, S.; Thuesen, C. A.; Weihe, H.; Bendix, J. Magnetic Properties of a Manganese(III) Chain with Monoatomic Bridges: Catena- $\text{MnF}(\text{Salen})$ . *Inorganic Chemistry* **2011**, *50*, 5312–5314.
- (31) Ferraro, J. R.; Zipper, J.; Wozniak, W. Transition Metal(II) Complexes of the Azines. *Applied Spectroscopy* **1969**, *23*, 160–164.

- (32) Zusai, K.; Kusaka, T.; Ishida, T.; Feyerherm, R.; Steiner, M.; Nogami, T. Magnetism of Pyrimidine-Bridged Metal(II) Halide Complexes. *Molecular Crystals and Liquid Crystals Science and Technology. Section A. Molecular Crystals and Liquid Crystals* **2000**, *343*, 127–132.
- (33) Feyerherm, R.; Loose, A.; Ishida, T.; Nogami, T.; Kreitlow, J.; Baabe, D.; Litterst, F. J.; Süllow, S.; Klauss, H.-H.; Doll, K. Weak Ferromagnetism with Very Large Canting in a Chiral Lattice: Fe(Pyrimidine)<sub>2</sub>Cl<sub>2</sub>. *Physical Review B* **2004**, *69*, 134427.
- (34) Hashizume, D.; Takayama, R.; Nakayama, K.; Ishida, T.; Nogami, T.; Yasui, M.; Iwasaki, F. Dichlorobis(Pyrimidine-*N*)Cobalt(II) and Its Bromo Derivative. *Acta Crystallographica Section C Crystal Structure Communications* **1999**, *55*, 1793–1797.
- (35) Kreitlow, J.; Menzel, D.; Wolter, A. U. B.; Schoenes, J.; Süllow, S.; Feyerherm, R.; Doll, K. Pressure Dependence of C<sub>4</sub>N<sub>2</sub>H<sub>4</sub>-Mediated Superexchange in XCl<sub>2</sub>(C<sub>4</sub>N<sub>2</sub>H<sub>4</sub>)<sub>2</sub> (X = Fe, Co, Ni). *Physical Review B* **2005**, *72*, 134418.
- (36) Cotton, F. A.; Daniels, L. M.; Feng, X.; Maloney, D. J.; Murillo, C. A.; Zúñiga, L. A. Experimental and Theoretical Study of a Paradigm Jahn-Teller Molecule, All-*Trans*-CrCl<sub>2</sub>(H<sub>2</sub>O)<sub>2</sub>(Pyridine)<sub>2</sub>, and the Related *Trans*-CrCl<sub>2</sub>(Pyridine)<sub>4</sub>·acetone. *Inorganica Chimica Acta* **1995**, *235*, 21–28.
- (37) Johnston, D. C. Unified Molecular Field Theory for Collinear and Noncollinear Heisenberg Antiferromagnets. *Physical Review B* **2015**, *91*, 064427.
- (38) Gazzoli, D.; Occhiuzzi, M.; Cimino, A.; Minelli, G.; Valigi, M. Chromium Oxidation States and XPS Analysis of the Chromia/Zirconia System. *Surface and Interface Analysis* **1992**, *18*, 315–322.
- (39) Campbell, B. J.; Stokes, H. T.; Tanner, D. E.; Hatch, D. M. ISODISPLACE: A Web-Based Tool for Exploring Structural Distortions. *Journal of Applied Crystallography* **2006**, *39*, 607–614.

- (40) Cracknell, A. P.; Davies, B.; Miller, S. C.; Love, W. F. *Kronecker Product Tables*; IFI/Plenum: New York, 1979; Vol. 1.
- (41) Toth, S.; Lake, B. Linear Spin Wave Theory for Single-Q Incommensurate Magnetic Structures. *Journal of Physics: Condensed Matter* **2015**, *27*, 166002.
- (42) Balucani, U.; Tognetti, V.; Pini, M. G. Kinematic Consistency in Anisotropic Ferromagnets. *Journal of Physics C: Solid State Physics* **1979**, *12*, 5513–5517.
- (43) Ciofini, I.; Daul, C. A. DFT Calculations of Molecular Magnetic Properties of Coordination Compounds. *Coordination Chemistry Reviews* **2003**, *238–239*, 187–209.
- (44) Tkatchenko, A.; DiStasio, R. A.; Car, R.; Scheffler, M. Accurate and Efficient Method for Many-Body van Der Waals Interactions. *Physical Review Letters* **2012**, *108*, 236402.
- (45) Formalik, F.; Fischer, M.; Rogacka, J.; Firlej, L.; Kuchta, B. Benchmarking of GGA Density Functionals for Modeling Structures of Nanoporous, Rigid and Flexible MOFs. *The Journal of Chemical Physics* **2018**, *149*, 064110.
- (46) Rhee, J. Y.; Singh, N. Electronic Structures and Optical Properties of Spinel  $\text{ZnCr}_2\text{O}_4$ . *Journal of the Korean Physical Society* **2010**, *57*, 1233–1237.
- (47) Wang, L.; Maxisch, T.; Ceder, G. Oxidation Energies of Transition Metal Oxides within the GGA+U Framework. *Physical Review B* **2006**, *73*, 195107.
- (48) Heyd, J.; Scuseria, G. E.; Ernzerhof, M. Hybrid Functionals Based on a Screened Coulomb Potential. *The Journal of Chemical Physics* **2003**, *118*, 8207–8215.
- (49) Janesko, B. G.; Henderson, T. M.; Scuseria, G. E. Screened Hybrid Density Functionals for Solid-State Chemistry and Physics. *Physical Chemistry Chemical Physics* **2009**, *11*, 443–454.
- (50) Zhu, X.; Edström, A.; Ederer, C. Magnetic Exchange Interactions in  $\text{SrMnO}_3$ . *Physical Review B* **2020**, *101*, 064401.

- (51) Rutter, M. J. C2x: A Tool for Visualisation and Input Preparation for Castep and Other Electronic Structure Codes. *Computer Physics Communications* **2018**, *225*, 174–179.
- (52) Butcher, R. T.; Landee, C. P.; Turnbull, M. M.; Xiao, F. Rectangular Two-Dimensional Antiferromagnetic Systems: Analysis of Copper(II) Pyrazine Dibromide and Dichloride. *Inorganica Chimica Acta* **2008**, *361*, 3654–3658.
- (53) Manson, J. L. et al. Structural, Electronic, and Magnetic Properties of Quasi-1D Quantum Magnets  $[\text{Ni}(\text{HF}_2)(\text{Pyz})_2]\text{X}$  ( $\text{Pyz}$  = Pyrazine;  $\text{X} = \text{PF}_6^-$ ,  $\text{SbF}_6^-$ ) Exhibiting Ni-FHF-Ni and Ni-pyz-Ni Spin Interactions. *Inorganic Chemistry* **2011**, *50*, 5990–6009.
- (54) Dos Santos, L. H. R.; Lanza, A.; Barton, A. M.; Brambleby, J.; Blackmore, W. J. A.; Goddard, P. A.; Xiao, F.; Williams, R. C.; Lancaster, T.; Pratt, F. L.; Blundell, S. J.; Singleton, J.; Manson, J. L.; Macchi, P. Experimental and Theoretical Electron Density Analysis of Copper Pyrazine Nitrate Quasi-Low-Dimensional Quantum Magnets. *Journal of the American Chemical Society* **2016**, *138*, 2280–2291.
- (55) Kubus, M.; Lanza, A.; Scatena, R.; Dos Santos, L. H. R.; Wehinger, B.; Casati, N.; Fiolka, C.; Keller, L.; Macchi, P.; Rüegg, C.; Krämer, K. W. Quasi-2D Heisenberg Antiferromagnets  $[\text{CuX}(\text{Pyz})_2](\text{BF}_4)$  with  $\text{X} = \text{Cl}$  and  $\text{Br}$ . *Inorganic Chemistry* **2018**, *57*, 4934–4943.
- (56) Perlepe, P.; Oyarzabal, I.; Pedersen, K. S.; Negrier, P.; Mondieig, D.; Rouzières, M.; Hillard, E. A.; Wilhelm, F.; Rogalev, A.; Sutura, E. A.; Mathonière, C.; Clérac, R.  $\text{Cr}(\text{Pyrazine})_2(\text{OSO}_2\text{CH}_3)_2$ : A Two-Dimensional Coordination Polymer with an Antiferromagnetic Ground State. *Polyhedron* **2018**, *153*, 248–253.
- (57) Näther, C.; Wöhlert, S.; Boeckmann, J.; Wriedt, M.; Jeß, I. A Rational Route to Coordination Polymers with Condensed Networks and Cooperative Magnetic Properties. *Zeitschrift für anorganische und allgemeine Chemie* **2013**, *639*, 2696–2714.

- (58) Wriedt, M.; Jeß, I.; Näther, C. Synthesis, Crystal Structure, and Thermal and Magnetic Properties of New Transition Metal-Pyrazine Coordination Polymers. *European Journal of Inorganic Chemistry* **2009**, 2009, 1406–1413.
- (59) Näther, C.; Greve, J. Thermal Decomposition Reactions as an Alternative Tool for the Preparation of New Coordination Polymers: Synthesis, Crystal Structure, Thermal and Magnetic Properties of Poly[Bis(Thiocyanato-N)-Bis( $M_2$ -Pyrazine-N,N')-Manganese(II)] and Poly[Bis( $M_2$ -Thiocyanato-N,S)-( $M_2$ -Pyrazine-N,N'-Manganese(II))]. *Journal of Solid State Chemistry* **2003**, 176, 259–265.
- (60) Lloret, F.; Julve, M.; Cano, J.; Munno, G. D. Topology and Spin Polarization in Sheet-like Metal(II) Polymers:  $[ML_2X_2]$  ( $M = \text{Mn, Fe, Co or Ni}$ ,  $L = \text{Pyrimidine or Pyrazine}$  and  $X = \text{NCS or NCO}$ ). *Molecular Crystals and Liquid Crystals Science and Technology. Section A. Molecular Crystals and Liquid Crystals* **1999**, 334, 569–585.
- (61) Lloret, F.; Munno, G. D.; Julve, M.; Cano, J.; Ruiz, R.; Caneschi, A. Spin Polarization and Ferromagnetism in Two-Dimensional Sheetlike Cobalt(II) Polymers:  $[\text{Co}(\text{L})_2(\text{NCS})_2]$  ( $\text{L} = \text{Pyrimidine or Pyrazine}$ ). *Angewandte Chemie International Edition* **1998**, 37, 135–138.
- (62) Wriedt, M.; Sellmer, S.; Näther, C. Thermal Decomposition Reactions as Tool for the Synthesis of New Metal Thiocyanate Diazine Coordination Polymers with Cooperative Magnetic Phenomena. *Inorganic Chemistry* **2009**, 48, 6896–6903.
- (63) Wehinger, B. et al. Giant Pressure Dependence and Dimensionality Switching in a Metal-Organic Quantum Antiferromagnet. *Physical Review Letters* **2018**, 121, 117201.
- (64) Scarborough, C. C.; Sproules, S.; Doonan, C. J.; Hagen, K. S.; Weyhermüller, T.; Wieghardt, K. Scrutinizing Low-Spin Cr(II) Complexes. *Inorganic Chemistry* **2012**, 51, 6969–6982.

- (65) Assary, R. S.; Brushett, F. R.; Curtiss, L. A. Reduction Potential Predictions of Some Aromatic Nitrogen-Containing Molecules. *RSC Advances* **2014**, *4*, 57442–57451.
- (66) Winkelmann, M.; Welz, D.; Baehr, M.; Hinz, D. J.; Dedেকে, T.; Urland, W.; Meyer, G. Magnetic Ordering and Low Magnetic Moment in the Quasi-1d Antiferromagnet  $\text{Na}_2\text{TiCl}_4$ . *Journal of Magnetism and Magnetic Materials* **1995**, *140–144*, 1667–1668.
- (67) Hirakawa, K.; Yoshizawa, H.; Ubukoshi, K. Magnetic and Neutron Scattering Study of One-Dimensional Heisenberg Antiferromagnet  $\text{CsVCl}_3$ . *Journal of the Physical Society of Japan* **1982**, *51*, 1119.
- (68) Cliffe, M. J.; Lee, J.; Paddison, J. A. M.; Schott, S.; Mukherjee, P.; Gaultois, M. W.; Manuel, P.; Sirringhaus, H.; Dutton, S. E.; Grey, C. P. Low-Dimensional Quantum Magnetism in  $\text{Cu}(\text{NCS})_2$ : A Molecular Framework Material. *Physical Review B* **2018**, *97*, 144421.
- (69) Kmety, C. R.; Huang, Q.; Lynn, J. W.; Erwin, R. W.; Manson, J. L.; McCall, S.; Crow, J. E.; Stevenson, K. L.; Miller, J. S.; Epstein, A. J. Noncollinear Antiferromagnetic Structure of the Molecule-Based Magnet  $\text{Mn}[\text{N}(\text{CN})_2]_2$ . *Physical Review B* **2000**, *62*, 5576–5588.
- (70) Granroth, G. E.; Meisel, M. W.; Chaparala, M.; Jolicoeur, T.; Ward, B. H.; Talham, D. R. Experimental Evidence of a Haldane Gap in an  $S = 2$  Quasi-linear Chain Antiferromagnet. *Physical Review Letters* **1996**, *77*, 1616–1619.
- (71) Itoh, S.; Tanaka, H.; Bull, M. J. Classical Properties in Spin Dynamics in the  $S = 2$  One-Dimensional Heisenberg Antiferromagnet,  $\text{CsCrCl}_3$ . *Journal of the Physical Society of Japan* **2002**, *71*, 1148–1153.
- (72) Manson, J. L. et al. Enhancing Easy-Plane Anisotropy in Bespoke  $\text{Ni}(\text{II})$  Quantum Magnets. *Polyhedron* **2020**, *180*, 114379.

- (73) López-Cabrelles, J.; Mañas-Valero, S.; Vitórica-Yrezábal, I. J.; Bereciartua, P. J.; Rodríguez-Velamazán, J. A.; Waerenborgh, J. C.; Vieira, B. J. C.; Davidovikj, D.; Steeneken, P. G.; van der Zant, H. S. J.; Mínguez Espallargas, G.; Coronado, E. Isorecticular Two-Dimensional Magnetic Coordination Polymers Prepared through Pre-Synthetic Ligand Functionalization. *Nature Chemistry* **2018**, *10*, 1001–1007.
- (74) Coelho, A. A. TOPAS and TOPAS-Academic: An Optimization Program Integrating Computer Algebra and Crystallographic Objects Written in C++. *Journal of Applied Crystallography* **2018**, *51*, 210–218.
- (75) Dolomanov, O. V.; Bourhis, L. J.; Gildea, R. J.; Howard, J. a. K.; Puschmann, H. OLEX2: A Complete Structure Solution, Refinement and Analysis Program. *Journal of Applied Crystallography* **2009**, *42*, 339–341.
- (76) Sheldrick, G. M. SHELXT – Integrated Space-Group and Crystal-Structure Determination. *Acta Crystallographica Section A: Foundations and Advances* **2015**, *71*, 3–8.
- (77) Sheldrick, G. M. Crystal Structure Refinement with SHELXL. *Acta Crystallographica Section C: Structural Chemistry* **2015**, *71*, 3–8.
- (78) Bain, G. A.; Berry, J. F. Diamagnetic Corrections and Pascal’s Constants. *Journal of Chemical Education* **2008**, *85*, 532.
- (79) Smith, D. R.; Fickett, F. R. Low-Temperature Properties of Silver. *Journal of Research of the National Institute of Standards and Technology* **1995**, *100*, 119–171.
- (80) Bewley, R. I.; Taylor, J. W.; Bennington, S. M. LET, a Cold Neutron Multi-Disk Chopper Spectrometer at ISIS. *Nuclear Instruments and Methods in Physics Research Section A: Accelerators, Spectrometers, Detectors and Associated Equipment* **2011**, *637*, 128–134.

- (81) Russina, M.; Mezei, F. First Implementation of Repetition Rate Multiplication in Neutron Spectroscopy. *Nuclear Instruments and Methods in Physics Research Section A: Accelerators, Spectrometers, Detectors and Associated Equipment* **2009**, *604*, 624–631.
- (82) Russina, M.; Mezei, F. Implementation of Repetition Rate Multiplication in Cold, Thermal and Hot Neutron Spectroscopy. *Journal of Physics: Conference Series* **2010**, *251*, 012079.
- (83) Arnold, O. et al. Mantid—Data Analysis and Visualization Package for Neutron Scattering and  $\mu$  SR Experiments. *Nuclear Instruments and Methods in Physics Research Section A: Accelerators, Spectrometers, Detectors and Associated Equipment* **2014**, *764*, 156–166.
- (84) Windsor, C. G. *Pulsed Neutron Scattering*; Taylor & Francis; Halsted Press: London; New York, 1981.
- (85) Clark, S. J.; Segall, M. D.; Pickard, C. J.; Hasnip, P. J.; Probert, M. I. J.; Refson, K.; Payne, M. C. First Principles Methods Using CASTEP. *Zeitschrift für Kristallographie - Crystalline Materials* **2005**, *220*, 567–570.
- (86) Monkhorst, H. J.; Pack, J. D. Special Points for Brillouin-zone Integrations. *Physical Review B* **1976**, *13*, 5188–5192.
- (87) Vanderbilt, D. Soft Self-Consistent Pseudopotentials in a Generalized Eigenvalue Formalism. *Physical Review B* **1990**, *41*, 7892–7895.
- (88) Morris, A. J.; Nicholls, R. J.; Pickard, C. J.; Yates, J. R. OptaDOS: A Tool for Obtaining Density of States, Core-Level and Optical Spectra from Electronic Structure Codes. *Computer Physics Communications* **2014**, *185*, 1477–1485.
- (89) Evans, M. L.; Morris, A. J. Matador: A Python Library for Analysing, Curating and



Performing High-Throughput Density-Functional Theory Calculations. *Journal of Open Source Software* **2020**, 5, 2563.